PERGAMON

International Journal of Heat and Mass Transfer 45 (2002) 1493–1511

International Journal of HEAT and MASS TRANSFER

www.elsevier.com/locate/ijhmt

MHD free convection in a liquid-metal filled cubic enclosure. II. Internal heating

Ivan Di Piazza [1], Michele Ciofalo *

Dipartimento di Ingegneria Nucleare, Università degli Studi di Palermo, Viale delle Scienze, I-90128 Palermo, Italy

Received 24 July 2000; received in revised form 6 July 2001

Abstract

The buoyancy-driven magnetohydrodynamic flow in a liquid-metal filled cubic enclosure with internal heat generation was investigated by three-dimensional numerical simulation. The enclosure was volumetrically heated by a uniform power density and was cooled along two opposite vertical walls, all other walls being adiabatic. A uniform magnetic field was applied orthogonally to the gravity vector and to the temperature gradient (i.e., parallel to the isothermal walls). The Prandtl number was 0.0321 (characteristic of Pb–17Li at 573 K); the Rayleigh number was made to vary from 10^5 to 10^7, the Hartmann number between 10^2 and 10^3 and the electrical conductance of the walls between 0 and infinity. The Navier–Stokes equations, in conjunction with a scalar transport equation for the fluid's enthalpy and with the Poisson equation for the electrical potential, were solved by a finite volume method using the CFD package CFX-4 with some necessary adaptations. Steady-state conditions were assumed. In all cases, a three-dimensional flow with complex secondary motions and a complex current pattern was established. The effects of Hartmann number, wall conductance ratio and Rayleigh number were discussed and results were compared with those previously obtained for fully developed flow in an infinitely tall, internally heated channel of square cross-section. The related case of a *differentially* heated cubic enclosure is discussed in a companion paper.

1. Introduction and previous work

Within the separated-cooled concept for the liquid-metal breeder blanket of a power fusion reactor [1], the problem arises of understanding and characterizing buoyant flows in a low Prandtl number fluid under the influence of a strong magnetic field.

In a previous paper [2], a general computational approach to MHD problems using an advanced CFD package with some necessary modifications was described. The method was validated against asymptotic results [3] for the case of fully developed buoyant flow induced by differential heating at two opposite walls or by internal heat generation. The use of a general purpose package in MHD modelling opens the possibility of numerical simulations being performed for complex geometries of direct engineering interest.

A companion paper [4] describes the application of the above general approach to MHD buoyant flow in a cubic enclosure with *differential* heating at two of the walls, the remaining four walls being adiabatic. In the present work, the study is extended to the case of a cubic enclosure with volumetric power generation (*internal* heating).

2. Model and computational methods

The configuration studied here (cubic enclosure of side length D with gravity vector, magnetic field, and temperature gradient orthogonal to one another and to the walls) is sketched in Fig. 1(a). The temperature gradient is due to internal heating in the presence of two opposite cold walls at $x = \pm 0.5$ and thus is directed along x. The magnetic field is directed along y.

The Rayleigh number is defined here as

$$Ra = g\beta q D^5/(\lambda \nu \alpha) \tag{1}$$

* Corresponding author. Tel.: +39-091-232-257/228; fax +39-091-232-215.

E-mail address: ciofalo@din.din.unipa.it (M. Ciofalo).

[1] Present address: CRS4, VI Strada Ovest, Z.I. Macchiareddu, I-09010 Uta (Cagliari), Italy.

0017-9310/02/$ - see front matter © 2002 Published by Elsevier Science Ltd.
PII: S0017-9310(01)00253-8

Nomenclature

$\mathbf{B}$ (B)	magnetic induction vector (module) (T)
c_w	wall conductance ratio, $(\sigma_w t_w)/(\sigma D)$ (dimensionless)
D	side length of the enclosure (m)
$\mathbf{g}$ (g)	gravity acceleration vector (module) (m s^{-2})
$\mathbf{j}$ (j)	current density vector (module) normalized by $j_0 = \sigma u_0 B$ (dimensionless)
M	Hartmann number, $DB(\sigma/\mu)^{1/2}$ (dimensionless)
Nu_1	first Nusselt number for internal heating, $1/T_{max}$ (dimensionless)
Nu_2	second Nusselt number for internal heating, $(2/3)/\langle T\rangle$ (dimensionless)
p	pressure normalized by Dj_0B (dimensionless)
Pr	Prandtl number, v/α (dimensionless)
q	power density (W m^{-3})
q''	heat flux (W m^{-2})
Ra	Rayleigh number for internal heating, $g\beta qD^5/(\lambda v\alpha)$ (dimensionless)
Re_m	magnetic Reynolds number, $u_0 D\sigma\eta$ (dimensionless)
t_w	wall thickness (m)
T	dimensionless temperature, $(\vartheta - \vartheta_w)/\vartheta_c$ (dimensionless)
u_0	velocity scale, $(\alpha/D)(Ra/M^2)$ (m s^{-1})
$\mathbf{v}$ (u,v,w)	velocity vector (components) normalized by u_0 (dimensionless)
x,y,z	co-ordinates normalized by D (dimensionless)

Greek symbols

α	thermal diffusivity (m^2 s^{-1})
β	thermal expansion coefficient (K^{-1})
δ_H, δ_S	thickness of the Hartmann and side layers normalized by D (dimensionless)
η	magnetic permeability (Ω s m^{-1})
ϑ	temperature (K)
ϑ_c	conductive temperature, $(qD^2)/(8\lambda)$ (K)
φ	electrical potential normalized by Du_0B (dimensionless)
λ	thermal conductivity (W m^{-1} K^{-1})
μ	viscosity (N s m^{-2})
v	kinematic viscosity (m^2 s^{-1})
ρ	density (kg m^{-3})
σ	electrical conductivity (Ω m)$^{-1}$

Subscripts

H	Hartmann layer
S	side layer
w	wall

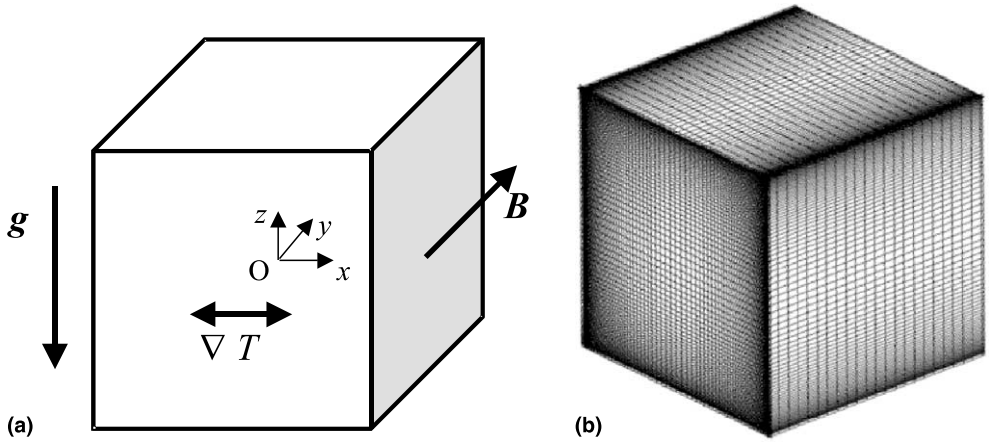

Fig. 1. (a) Sketch of the three-dimensional cubic enclosure; (b) computational grid.

in which β, λ, v and α are the fluid's thermal expansion coefficient, thermal conductivity, kinematic viscosity, and thermal diffusivity, respectively. The Hartmann number is defined as

$$M = DB(\sigma/\mu)^{1/2} \tag{2}$$

in which σ, ρ and $\mu = \rho v$ are the fluid's electrical conductivity, density, and viscosity. It can be shown that M^2 represents the ratio of electromagnetic to viscous forces.

The walls normal to the magnetic field are called Hartmann walls. In the associated boundary layers, the

velocity profile is basically determined by a balance between Lorentz and viscous forces, and their thickness δ_H scales as M^{-1}. The walls parallel to the magnetic field are called the side walls, and the associated boundary layers are called side layers; their thickness δ_S scales as $M^{-1/2}$ [5].

Under the assumption of a low magnetic Reynolds number $Re_m = u_0 D\sigma\eta$ (in which $u_0 = (\alpha/D)(Ra/M^2)$ is a characteristic velocity and η is the fluid's magnetic permeability), the induced magnetic field is negligible with respect to the applied field **B**. Such an inductionless flow is governed by the Navier–Stokes equations with the Lorentz force $\mathbf{J} \times \mathbf{B}$ added to the RHS. By using the Boussinesq approximation for buoyancy, assuming steady-state conditions and making all terms dimensionless as discussed below, these become

$$\frac{Gr}{M^4}(v \cdot \nabla)v = -\nabla p + \frac{1}{M^2}\nabla^2 v + j \times \hat{y} + \frac{1}{8}T\hat{z} \tag{3}$$

and are complemented by the continuity equation

$$\nabla \cdot v = 0. \tag{4}$$

The velocity vector $\mathbf{v} = (u, v, w)$ and the current density **j** are scaled, respectively, by u_0 and by $j_0 = \sigma v_0 B$. The dimensionless pressure p is the difference between the local and the hydrostatic pressure, scaled by Dj_0B. The dimensionless temperature T is the difference between the local temperature ϑ and the temperature of the cold (i.e., thermally active) walls, divided by the temperature scale (conductive temperature maximum) $\vartheta_c = qD^2/8\lambda$.

The current density is given by Ohm's law

$$\mathbf{j} = -\nabla\varphi + \mathbf{v} \times \hat{y} \tag{5}$$

together with the conservation of the electric charge

$$\nabla \cdot \mathbf{j} = 0. \tag{6}$$

The electrical potential φ is scaled by Du_0B. From Eqs. (5) and (6) a Poisson equation for φ is derived

$$\nabla^2\varphi = (\nabla \times \mathbf{v})\hat{y}. \tag{7}$$

The temperature distribution is governed by the enthalpy transport equation

$$Pe(v \cdot \nabla)T = \frac{1}{M^2}\nabla^2 T + 8, \tag{8}$$

where $Pe = Ra/M^2$ is the Péclet number. Note that the term 8 on the RHS accounts for internal heating and is not present in the case of a *differentially* heated cavity [4].

The boundary conditions for velocity are the usual no-slip conditions at the walls (see below, however, for the treatment of walls orthogonal to the magnetic field), while the thermal boundary conditions are

$$T = 0 \quad \text{for } x = \pm 0.5, \tag{9a}$$

$$\partial T/\partial y = 0 \quad \text{for } y = \pm 0.5, \tag{9b}$$

$$\partial T/\partial z = 0 \quad \text{for } z = \pm 0.5. \tag{9c}$$

The purely conductive solution is $T = 1 - 4x^2$.

The electrical boundary conditions are simply those expressing the continuity of electrical potential φ and electrical current $\mathbf{j} = -\sigma\nabla\varphi$ at the fluid–wall interface. In the special case of plane walls (as in the present example), by integration across the wall thickness t_w these can be reduced to the thin wall condition [6] expressing the conservation of electric charge in the plane of the wall

$$\mathbf{j} \cdot \mathbf{n} = c_w \nabla_w^2 \langle\varphi\rangle \tag{10}$$

in which $\langle\varphi\rangle$ is the mean value of φ across the wall, **n** is the inward-directed unity vector normal to the wall and ∇_w^2 is the two-dimensional Laplace operator in the plane of the wall. The constant c_w is the wall conductance ratio, $\sigma_w t_w/\sigma D$.

The governing equations (3), (4) and (7), (8), with the boundary conditions discussed above, were solved by a finite volume technique using the SIMPLEC pressure–velocity coupling algorithm [7] and the QUICK third-order discretization scheme for the advection terms. The CFD package CFX-4 [8] was used for the simulations, but some adaptations were required [9] since CFX-4 does not explicitly provide for MHD problems. In particular, the electrical potential equation was solved by using the elliptic solvers normally adopted in CFX-4 for the solution of scalar transport equations, appropriately modified so as not to include convection terms. This allowed the problem to be treated as a fully implicit fluid dynamics – scalar transport problem, without any explicit "outer" coupling between hydrodynamic and electrical quantities.

The resolution of the Hartmann layer was omitted by integrating analytically all equations across it as suggested by Leboucher [10]. Coherently, the dimensionless wall conductance c_w at the Hartmann walls was replaced by $c_w + \delta_H$, being $\delta_H = M^{-1}$ the conductance of the fluid layer. Near these walls, the first grid point in the fluid lay outside of the Hartmann layer, and the no-slip condition was replaced by a free slip condition (linear extrapolation of the velocity at the wall from the inner grid points).

As mentioned for the case of a differentially heated enclosure [4], the above model could easily be extended to more complex geometries, including the case of solid walls arbitrarily oriented with respect to the magnetic field. However, in this case the *local* wall conductance ratio should be written as $c_w + (M\mathbf{n}\hat{y})^{-1}$, according to the local thickness of the Hartmann layer along the wall surface [11].

In the MHD simulations reported here, a grid of $n_x \times n_y \times n_z = 90 \times 24 \times 90 = 194{,}400$ nodes was used,

with a non-equispaced distribution in the directions x and z orthogonal to the magnetic field, Fig. 1(b). The magnetic field direction y was resolved by a comparatively smaller number of points since the above-mentioned integral model was adopted for the Hartmann layers. Some simulations with no MHD effects were also

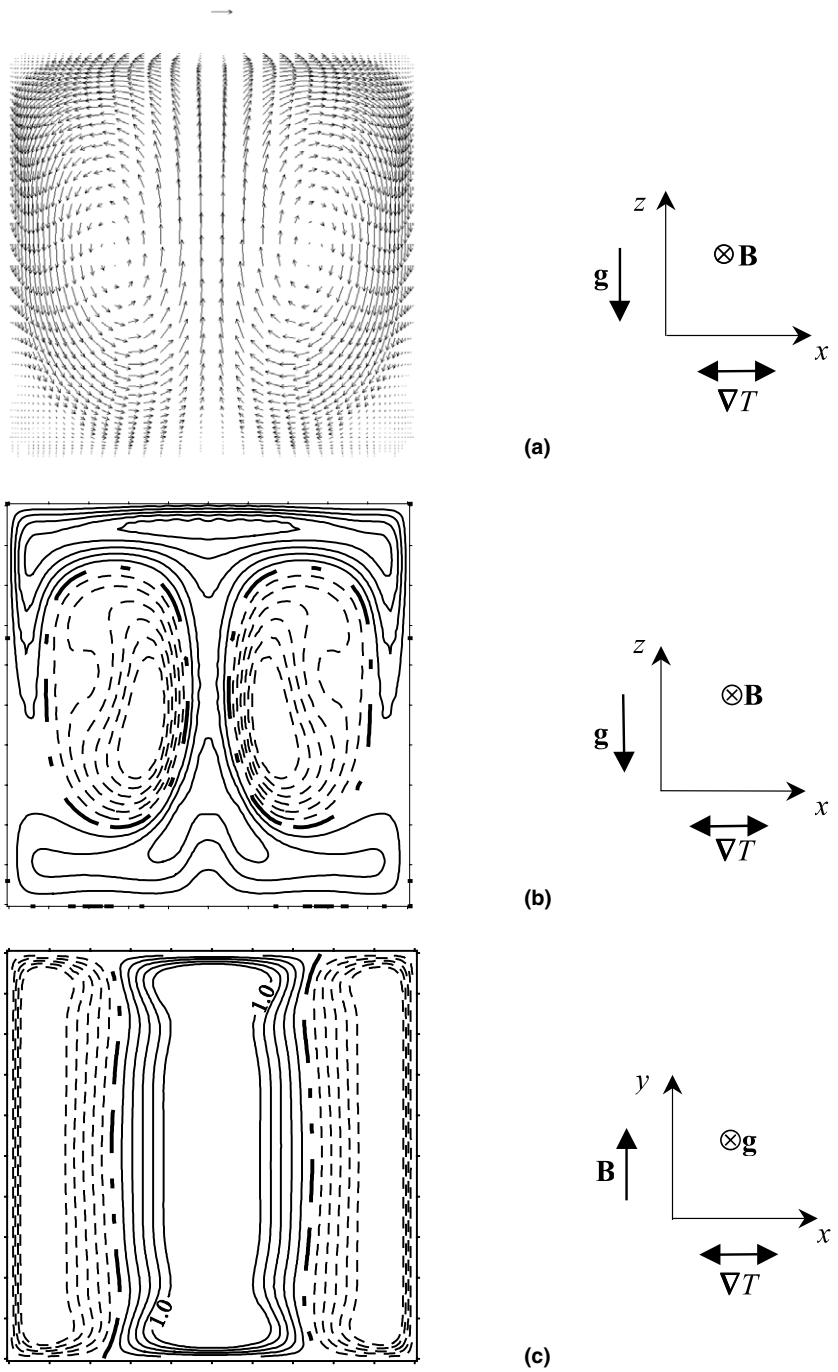

Fig. 2. Base flow (no MHD) for $Ra = 10^5$. Velocities are scaled as for $M = 100$. (a) Velocity vector plot in the plane $y = 0$; the (dimensionless) unity vector is shown. (b) Contours of the v velocity in the plane $y = -0.2$. Solid line: negative velocity; broken line: positive velocity; thick line: zero. (c) Contours of the vertical w velocity in the midplane $z = 0$. Solid line: upward flow; broken line: downward flow; thick line: zero.

performed; for these cases, a non-equispaced grid with $n_x \times n_y \times n_z = 60 \times 60 \times 60 = 216{,}000$ nodes was used.

1500 iterations at most were needed for a complete convergence of all variables; the convergence speed was thus higher than for the quasi-2D, fully developed, problem [2] and was only slightly affected by the conductivity of the walls, the Rayleigh number, or the Hartmann number. All simulations were run on a Pentium III-500 MHz computer with 256 Mbytes RAM; each test case typically required ~40 h of CPU time.

3. Base flow in the absence of MHD interactions

The buoyant flow in enclosures with internal heat generation has been studied for many years in different contexts ranging from plate tectonics to nuclear safety. Theoretical and experimental results have been reviewed, among others, by Kulacki and Richards [12].

For square enclosures and low Prandtl numbers ($Pr = 0.0321$), two-dimensional direct simulations have recently been presented by Arcidiacono et al. [13] in the range $Ra \approx 10^4$–10^8. Their results indicate that the flow is steady and bilaterally symmetric up to $Ra \approx 3 \times 10^5$; a pitchfork bifurcation, with spatial symmetry breaking, occurs at $3 \times 10^5 < Ra < 10^6$, a Hopf bifurcation to periodic flow at $10^6 < Ra < 2 \times 10^6$, and a final transition to chaotic flow at $2 \times 10^6 < Ra < 3 \times 10^6$.

For cubic enclosures, three-dimensional effects must be taken into account. In the case of *differential* heating, Davis [14] argued that the interaction of the main circulation roll with the side walls should give rise to a secondary flow with a velocity component parallel to the roll axis. Mallinson and de Vahl Davis [15] presented 3-D finite-difference numerical simulations for different aspect ratios, Prandtl numbers ranging from 0.2 to 100 and Rayleigh numbers ranging from 10^4 to 10^5. For an enclosure of aspect ratios 1:2:1 (x:y:z, see axis nomenclature in Fig. 1), they predicted characteristic toroidal circulation cells with the flow moving inward, i.e. toward the midplane $y = 0$, in the centre and outward, i.e., toward the side walls, at the periphery. A similar three-dimensional flow pattern was experimentally confirmed by the flow visualization studies of Hiller et al. [16], based on thermochromic liquid crystals suspended in water–glycerol mixtures filling a cubic enclosure ($Pr = 5.8$–$6000, Ra = 10^4$–2×10^7).

For internally heated two-dimensional enclosures, at sufficiently low Rayleigh number the base flow presents a central rising plume and two symmetric recirculation rolls. No previous detailed three-dimensional studies have been presented in the literature; however, by analogy with differentially heated enclosures [4], one may expect that *two* toroidal secondary flows will develop close to each side wall, with the fluid moving inward in the central regions of the main recirculation rolls and outward along the periphery.

These expectations are fully confirmed by the present simulations. Fig. 2 reports predictions obtained for $Ra = 10^5$. Fig. 2(a) is a vector plot of the main circulation in the midplane $y = 0$, showing a central rising plume, descending boundary layers along the cold vertical walls and two symmetric recirculation rolls. Fig. 2(b) reports contours of the v velocity in the plane $y = -0.2$; two symmetric toroidal cells can be clearly recognized, with fluid moving inward (from the side wall at $y = -0.5$ to the midplane at $y = 0$) near the centres of the main circulation rolls and moving outward in the peripheral region of each roll. Fig. 2(c) reports contours of the vertical velocity w in the midplane $z = 0$; these show that the main buoyant flow is fairly two-dimensional along the central half of the enclosure span, while end effects due to the influence of the side walls become significant only for $|y| \gtrsim 0.25$.

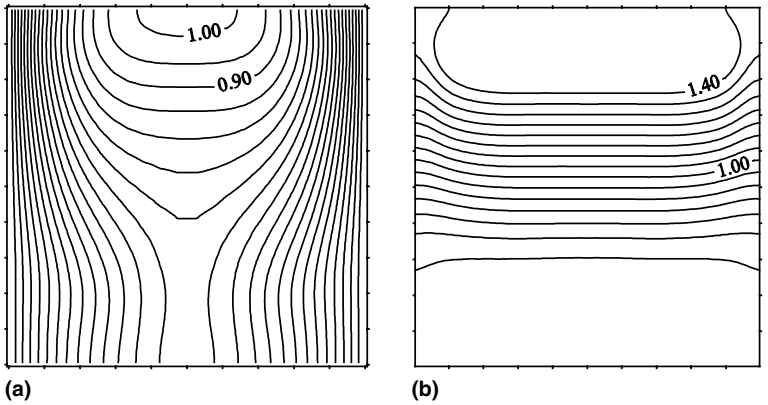

Fig. 3. Heat transfer for $Ra = 10^5$, base flow (no MHD). (a) Temperature in the midplane $y = 0$. (b) Normalized wall heat flux $q''/\langle q'' \rangle$ on a cold wall.

Some features of the thermal field in the cubic enclosure for the same Rayleigh number (10^5) and no MHD effects are illustrated in Fig. 3. Graph (a) shows the isotherms in the midplane $y = 0$; at the present low *Ra* only a moderate amount of vertical stratification is present, and is confined to the upper half of the

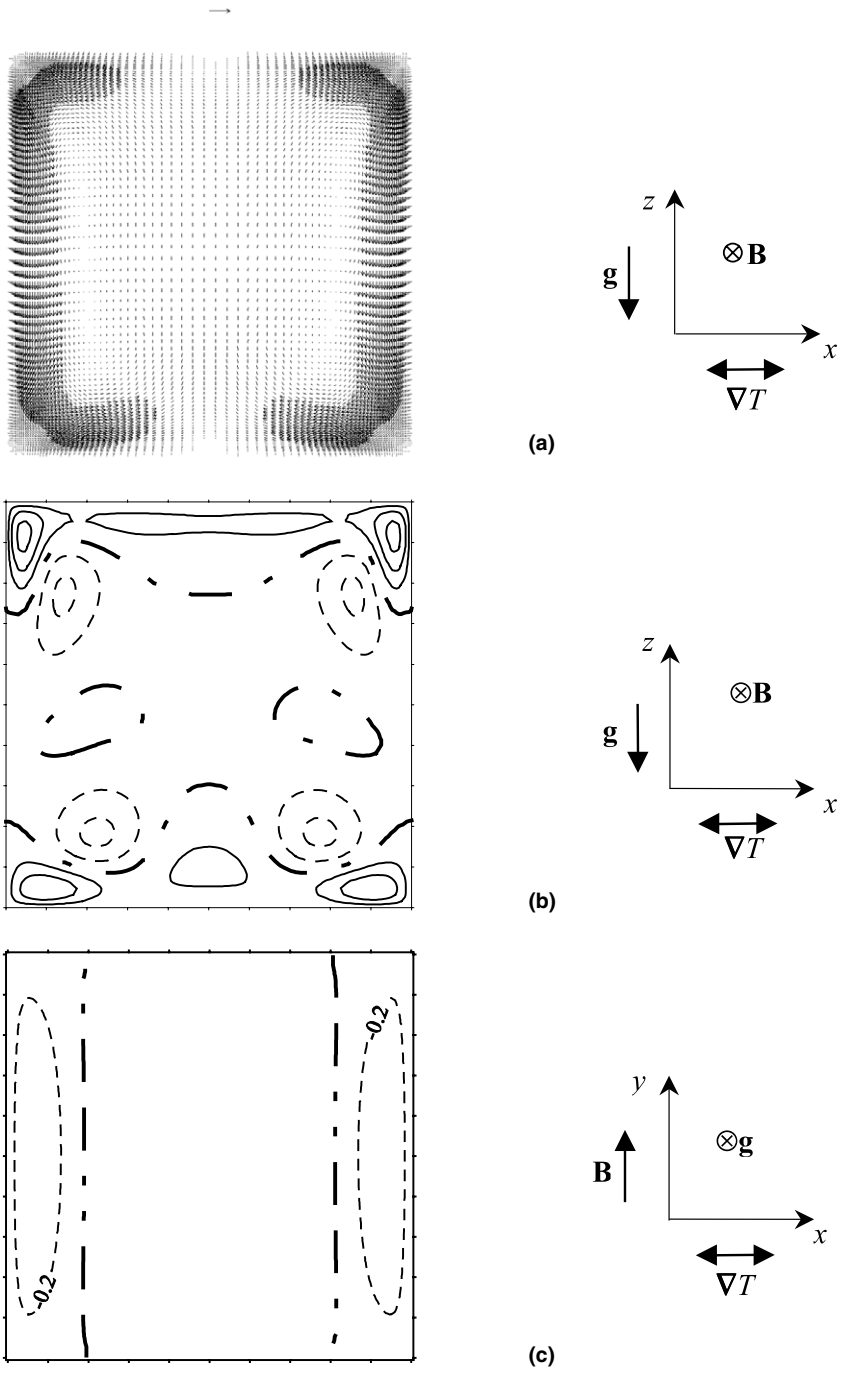

Fig. 4. MHD flow for $Ra = 10^5$, $M = 100$, $c_w \to \infty$. (a) Velocity vector plot in the plane $y = 0$; the (dimensionless) unity vector is shown. (b) Contours of the v velocity in the plane $y = -0.2$. Solid line: negative velocity; broken line: positive velocity; thick line: zero. (c) Contours of the vertical w velocity in the midplane $z = 0$. Solid line: upward flow; broken line: downward flow; thick line: zero.

enclosure; in the bottom half and in the regions close to the cold walls the thermal stratification is mainly horizontal, showing that most of the heat is transferred by conduction in the liquid metal. Fig. 3(b) reports contours of the wall heat flux (normalized by its mean value $qD/2$) along one of the cold walls; peak values of $\sim$1.4 are attained in the upper region of the wall while values below $\sim$0.7 are attained in the bottom half. Three-dimensional effects can be seen to regard only the end regions close to the side walls.

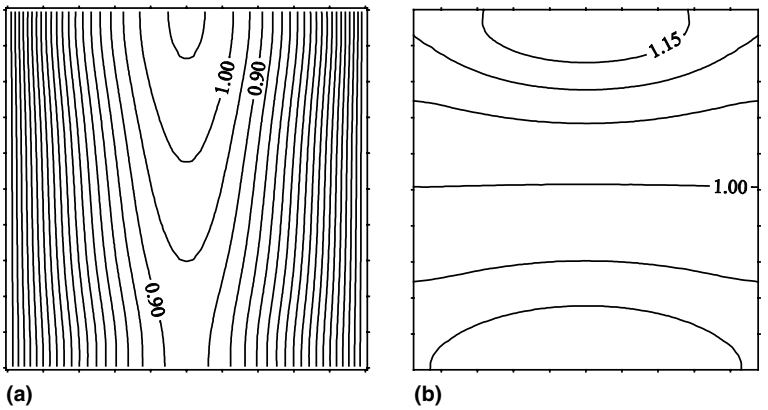

Fig. 5. Heat transfer for $Ra = 10^5,\ M = 100,\ c_w \to \infty$. (a) Temperature in the midplane $y = 0$. (b) Normalized wall heat flux $q''/\langle q''\rangle$ on a cold wall.

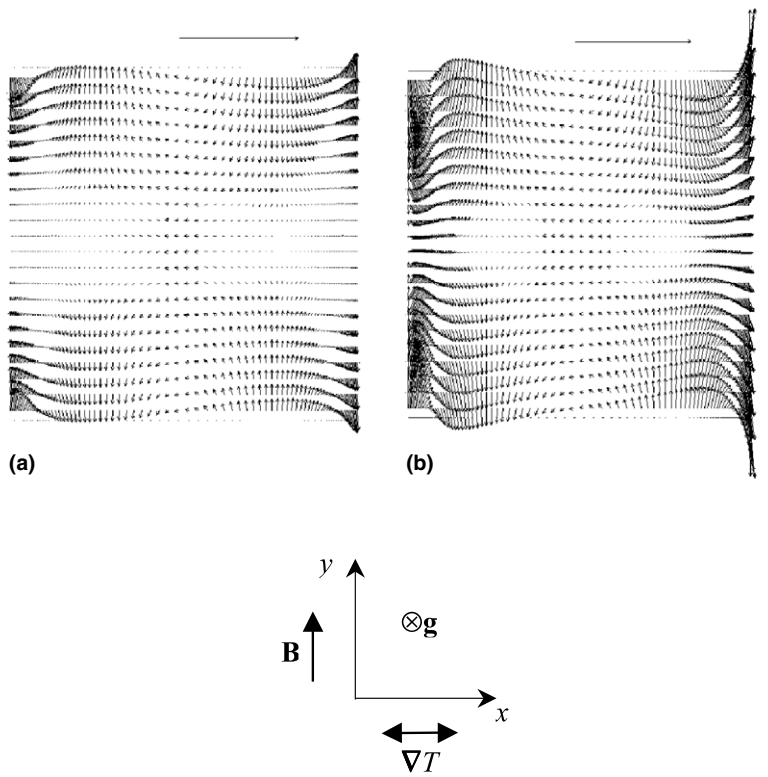

Fig. 6. Total current **j** in the midplane $z = 0$ for $c_w = 0.01,\ Ra = 10^5$. The unity (dimensionless) vector is shown above each plot. (a) $M = 100$; (b) $M = 1000$.

Three-dimensionality should also be carefully considered for its influence on flow regime stability and transitions. Again, the case of internally heated enclosures is poorly documented in the literature. For differentially heated enclosures, three-dimensional numerical simulations were presented by Janssen et al. [17] with $Pr = 0.71$ (gases) and Ra ranging from 10^5 to 10^8. Instability mechanisms, leading from steady-state to time-periodic and chaotic flow, and corresponding dominating frequencies, were found to be similar to those found in 2-D studies; transition to periodic flow was predicted for $Ra = 2.3 \times 10^6$, $\sim$10% *higher* than for a corresponding 2-D enclosure. On the other hand, Henkes and Le Quéré [18] conducted three-dimensional numerical simulations for a cavity of vertical aspect ratio 1 at $Pr = 0.71$ and Ra ranging from $\sim 10^6$ to $\sim 10^8$ using a spectral method with up to 109×109 Chebyshev modes in the vertical planes normal to the isothermal walls and nine Fourier modes along the depth, where periodic boundary conditions were enforced. For perfectly conducting horizontal walls, at $Ra = 1.8 \times 10^6$ the base steady solution was unstable to three-dimensional temperature perturbations having a wavelength of the order of D, while at the same Ra the solution was stable with respect to two-dimensional perturbations. When horizontal adiabatic walls were imposed, the critical Rayleigh numbers increased by almost two orders of magnitude, but also in this case three-dimensional perturbations turned out to be the most unstable.

These last results suggest that the critical Rayleigh numbers for transition to asymmetric, unsteady or chaotic solutions obtained by two-dimensional numerical simulations [13] may require significant cor-

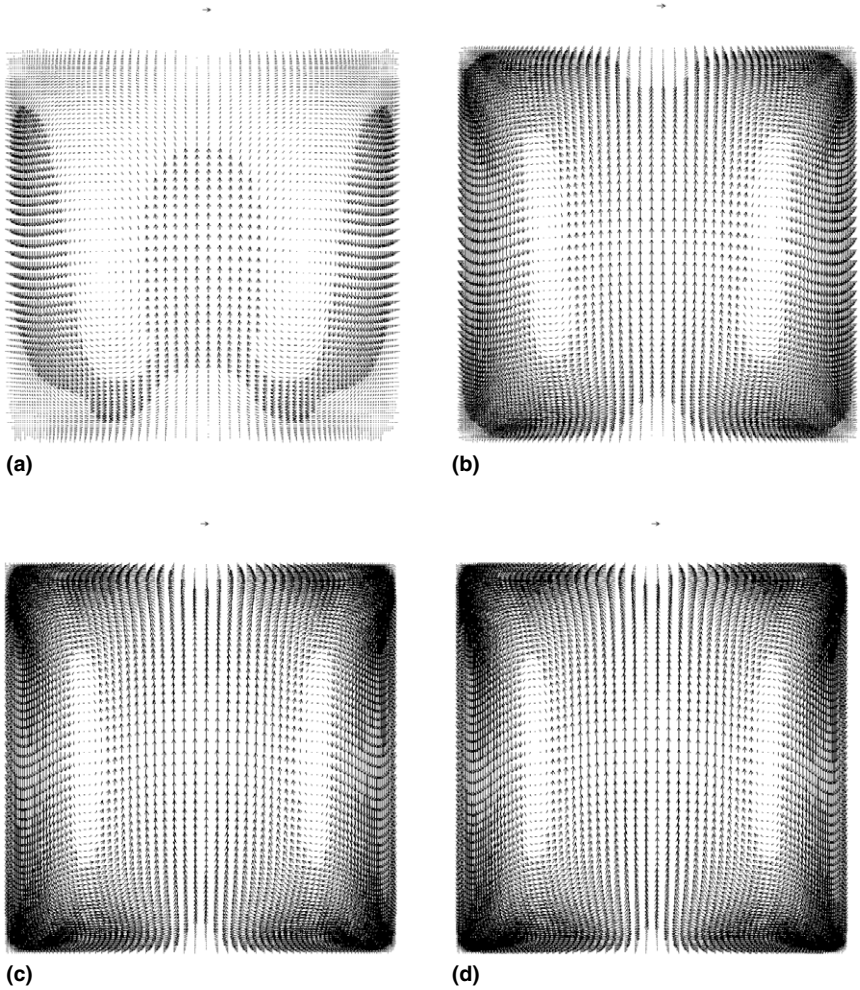

Fig. 7. Velocity vectors in the midplane $y = 0$ for $c_w = 0.01$, $Ra = 10^5$. The unity (dimensionless) vector is shown above each plot. (a) $M = 100$; (b) $M = 200$; (c) $M = 500$; (d) $M = 1000$.

rections for three-dimensional enclosures. However, the reference Rayleigh number for which the present base flow was computed (10^5) is sufficiently low for the flow to be assumed with confidence to be steady and bilaterally symmetric not only in 2-D, but also in 3-D enclosures.

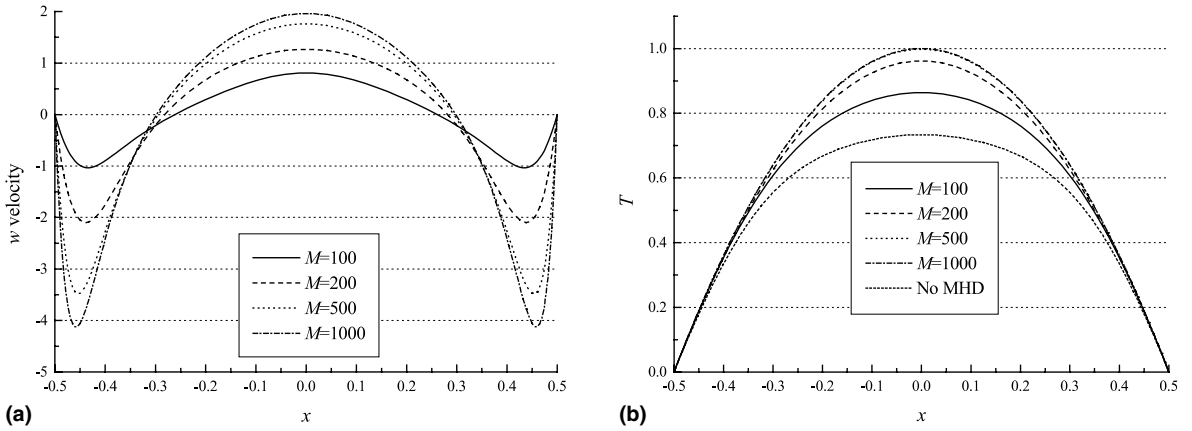

Fig. 8. Velocity (a) and temperature (b) profiles along the x axis for $c_w = 0.01$, $Ra = 10^5$. Velocities for "no MHD" are scaled as for $M = 100$.

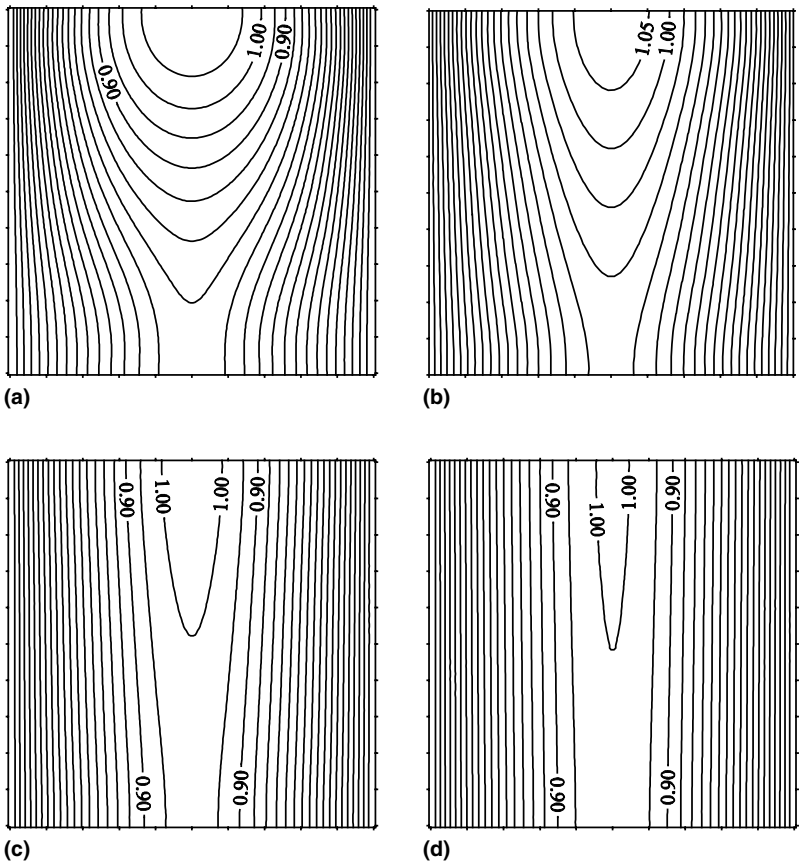

Fig. 9. Dimensionless temperature in the midplane $y = 0$ for $c_w = 0.01$, $Ra = 10^5$. (a) $M = 100$; (b) $M = 200$; (c) $M = 500$; (d) $M = 1000$.

4. MHD free convection flow

4.1. Review of the literature

A recent review of published results for convective magnetohydrodynamic flows in ducts and cavities was given by Müller and Bühler [19]. No computational work appears to have been presented on buoyant flows due to internal heat generation in fully three-dimensional configurations. Bühler [3] developed an asymptotic analysis for the MHD flow in a vertical rectangular duct, taking both differential heating and internal heating into consideration; but only for fully developed conditions in which convection plays essentially no role. Di Piazza and Bühler [2] studied the same configurations by the present numerical approach, based on the CFX-4 code [8], and were able to reproduce well the analytical results derived in [3].

In cubic enclosures, in contrast with the fully developed flow problem, convective terms are important and a fully three-dimensional flow occurs; exact solutions do not exist and neither numerical nor experimental results have been presented in the literature, so that the present computations can only be judged on the basis of physical coherence and by analogy with related configurations.

4.2. The case $Ra = 10^5, M = 100, c_w = \infty$ (perfectly conducting walls)

Typical MHD results will be shown here for a Rayleigh number of 10^5, a Hartmann number of 100 and perfectly conducting cavity walls ($c_w \to \infty$).

Fig. 4 illustrates some features of the flow field, and can be compared with Fig. 2 relative to the case with no MHD (in which velocities were scaled based on $M = 100$ for ease of comparison). The main circulation, see vector plot for the midplane $y = 0$ in Fig. 4(a), is characterized by peak velocities 3–4 times lower than in the base flow, and mainly consists of a peripheral belt of moving fluid, attached to the cavity walls and surrounding a core region where the fluid flows slowly upward. The rounded circulation cells characterizing the base flow, Fig. 2(a), are completely absent here.

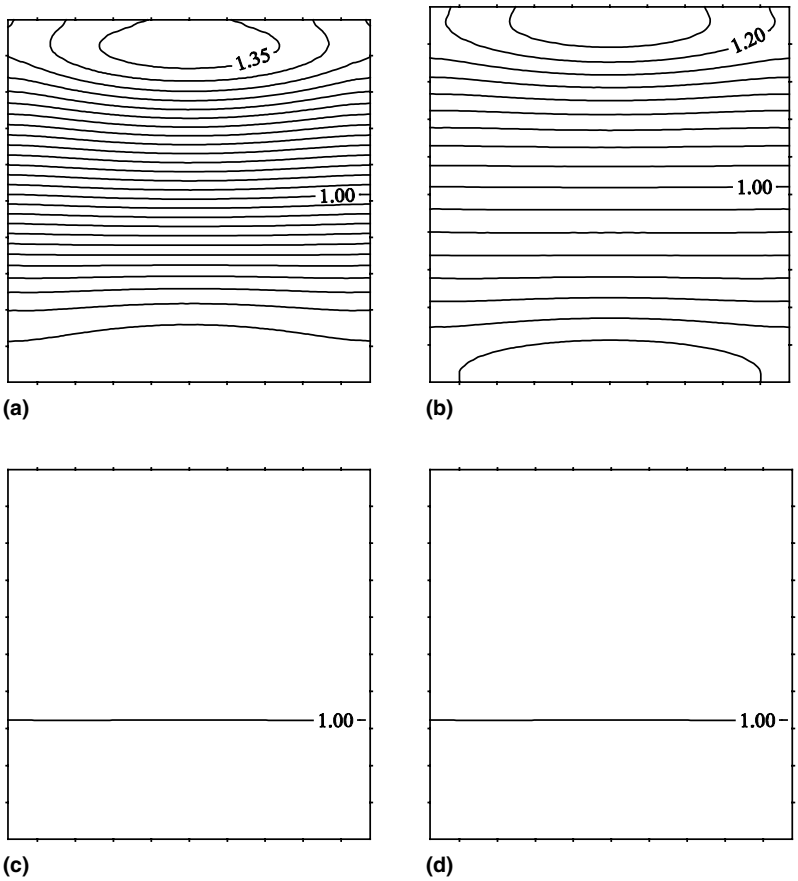

Fig. 10. Distribution of $q''/\langle q'' \rangle$ in the plane $y = 0$ for $c_w = 0.01$, $Ra = 10^5$. (a) $M = 100$; (b) $M = 200$; (c) $M = 500$; (d) $M = 1000$.

Contours of the v velocity component in the plane $y = -0.2$ are shown in Fig. 4(b). The toroidal cells of secondary circulation discussed for the base flow, Fig. 2(b), are absent here; secondary circulation normal to the constant-y planes is confined to the four corner regions of the enclosure.

The spanwise variation of the main (vertical) velocity component w is illustrated in Fig. 4(c). It can be observed that the null-w lines are almost straight along the spanwise y direction, indicating an almost 2-D flow which is little affected by the end (Hartmann) walls at $y = \pm 0.5$. This contrasts with the more marked spanwise variation exhibited by the base flow, Fig. 2(c), and shows that the effect of MHD interactions is to align vorticity with the magnetic field direction thus increasing the two-dimensionality of the flow.

The thermal field in the midplane $y = 0$ is shown for the present MHD case in Fig. 5(a); by comparison with the base flow results in Fig. 3(a), it can be observed that the temperature distribution is now much closer to the purely conductive one, with little vertical stratification. Vertical convection leads to the appearance of a top central region where the temperature markedly exceeds the purely conductive value (dimensionless $T > 1$), as observed in square cavities without MHD at much lower Rayleigh numbers [13]. The distribution of the wall heat flux on one of the active (cold) walls is shown in Fig. 5(b); q'' is normalized by its mean value $qD/2$. The distribution is considerably flatter than in the base flow, Fig. 3(b), with peak values of just ~ 1.15 in the top region of the wall.

4.3. The effect of the Hartmann number M

For a given value of the Rayleigh number ($Ra = 10^5$) and of the wall conductance ratio ($c_w = 10^{-2}$), the Hartmann number M was made to vary in order to clarify its influence on fluid flow and heat transfer.

Vector plots of the total current **j** in the midplane $z = 0$ are shown in Fig. 6 for $M = 100$ and 1000. The general pattern is similar for the two values of M, with side layer current jets parallel to the walls. The reason for these jets is that the conductance of the side layer (which scales as $M^{-1/2}$) is larger than the wall conductance c_w even for the higher value of the Hartmann number considered here ($M = 1000$); only when the wall

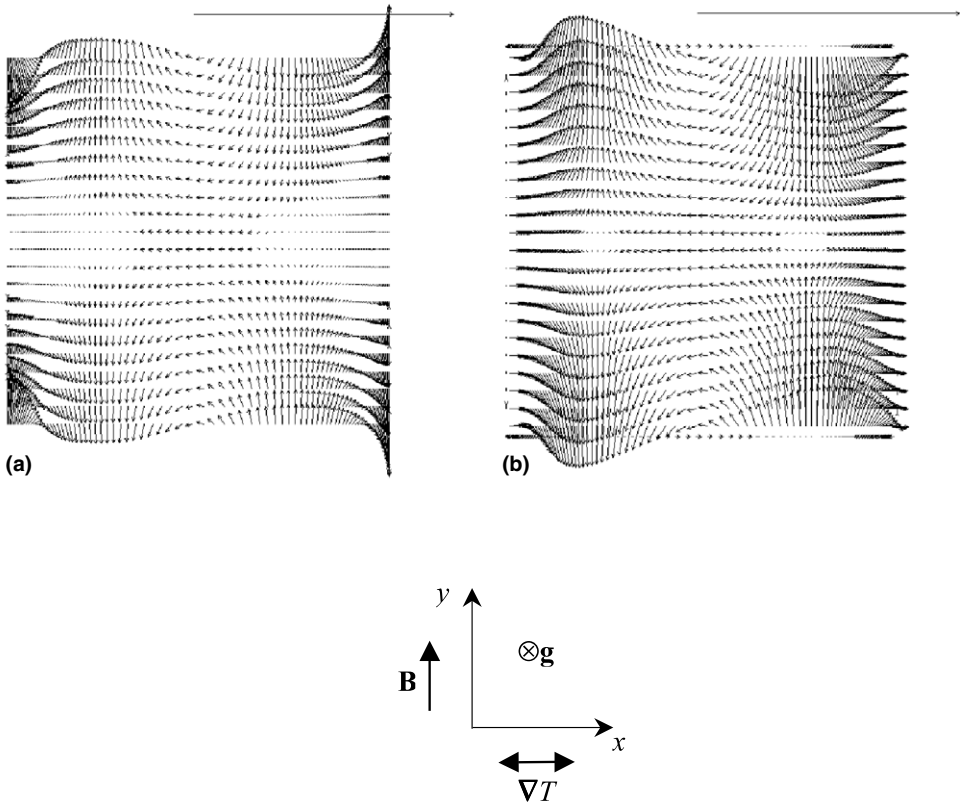

Fig. 11. Total current **j** in the midplane $z = 0$ for $M = 100$, $Ra = 10^5$. The unity (dimensionless) vector is shown above each plot. (a) $c_w = 0$; (b) $c_w \to \infty$.

conductance ratio becomes larger than the layer conductance, i.e. for higher M or lower c_w, current jets are no more present.

Fig. 7 shows velocity vector plots in the midplane $y = 0$ for $M = 100$, 200, 500, 1000 (a)–(d). The corresponding results for the purely hydrodynamic case (no MHD) were shown in Fig. 2(a). Each plot is scaled with its own scale $u_0 = (\alpha/D) \cdot (Ra/M^2)$. A remarkable damping effect can be observed as M increases, since velocities remain of the same order despite the fact that the velocity scale is much lower for high Hartmann numbers. Furthermore, the squareness of the circulation cells increase, and the thickness of the side boundary layers decreases as the Hartmann number increases.

Magnetic damping effects are also illustrated by the vertical velocity profiles along the x axis shown in Fig. 8(a) for $M = 100$–1000. Fig. 8(b) reports the dimensionless temperature profiles along the same axis; for the lower Hartmann numbers and for the purely hydrodynamic case, the presence of a vertical stratification keeps the maximum value of the distribution significantly lower than unity, whereas the T profile approaches the purely conductive parabolic distribution for $M = 1000$.

The influence of M on the temperature distribution is also evidenced in Fig. 9, where the isotherms in the midplane $y = 0$ are shown for $M = 100$–1000. Results for the case with no MHD interactions were reported in

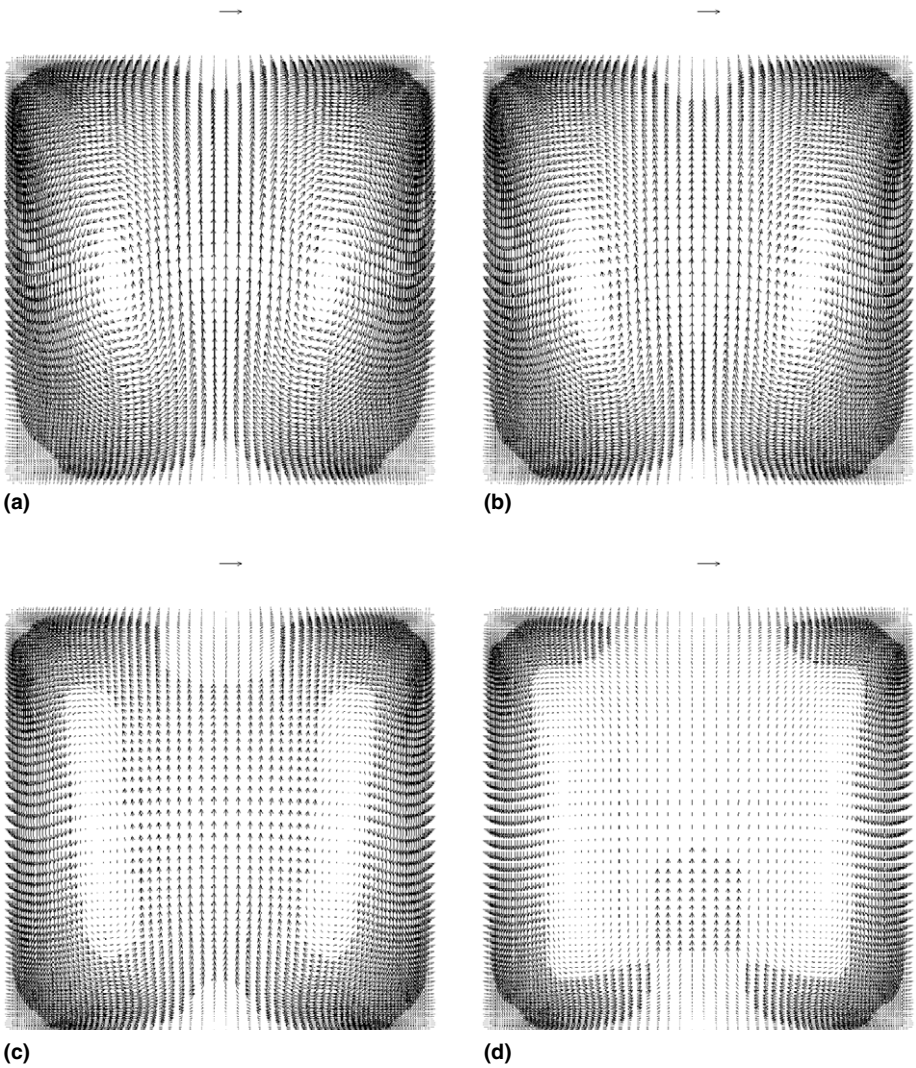

Fig. 12. Velocity vectors in the midplane $y = 0$ for $M = 100$, $Ra = 10^5$. The unity (dimensionless) vector is shown above each plot. (a) $c_w = 0$; (b) $c_w = 0.01$; (c) $c_w = 0.1$; (d) $c_w = 1$.

Fig. 3(a). For the higher values of M, (c) and (d), convection plays a minor role, and the distribution is mainly conductive with purely horizontal thermal stratification.

The suppression of convection can also be observed in the maps of the average heat flux on a cooling wall reported in Fig. 10. The maximum of ~1.5 attained in

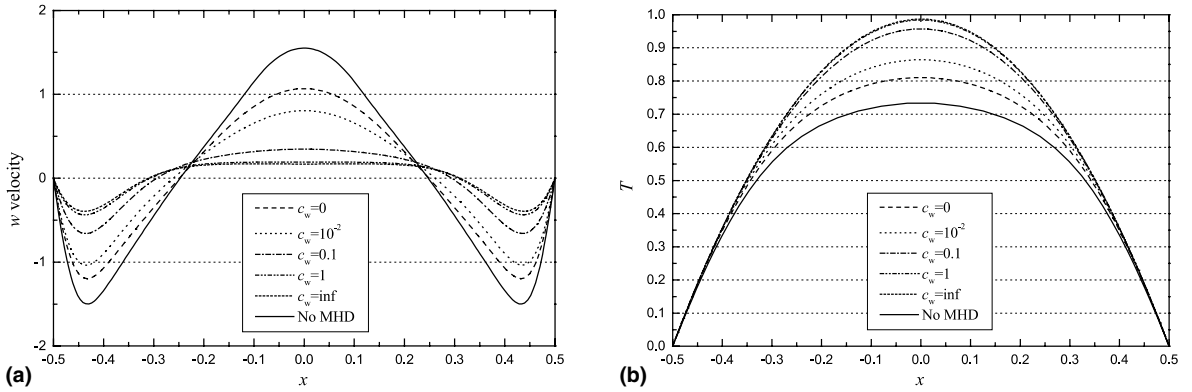

Fig. 13. Dimensionless velocity (a) and temperature (b) profiles along the x axis for $M = 100$, $Ra = 10^5$. Velocities for "no MHD" are scaled as for $M = 100$.

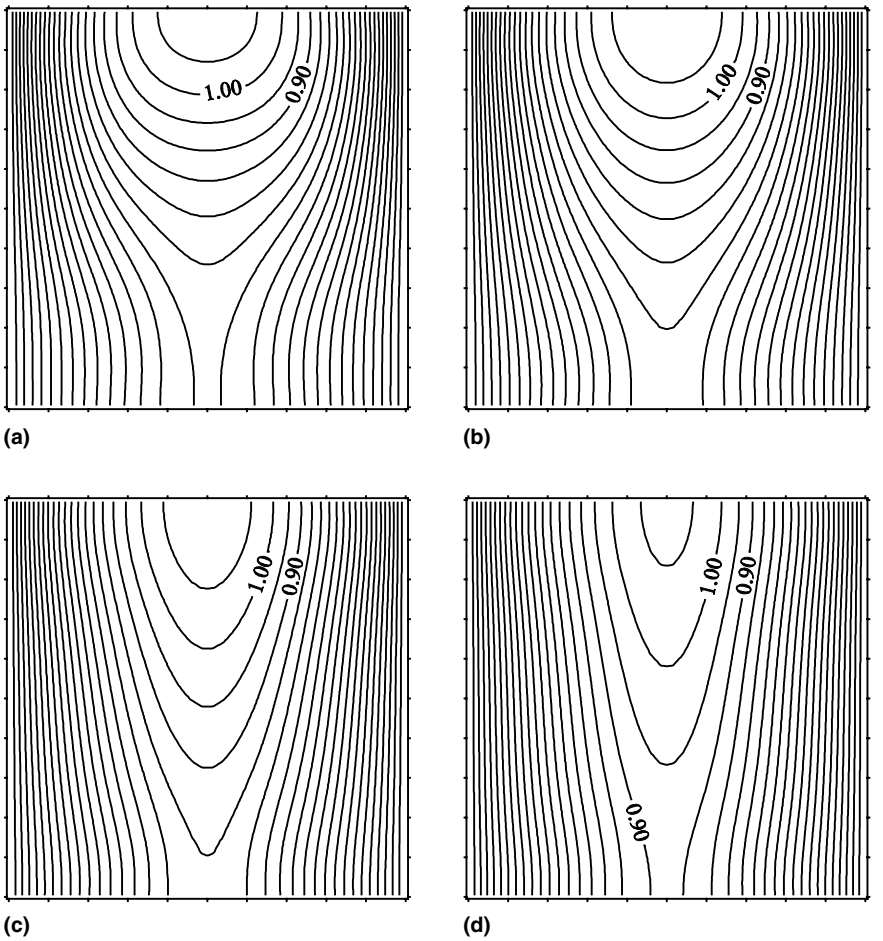

Fig. 14. Dimensionless temperature in the midplane $y = 0$ for $M = 100$, $Ra = 10^5$. (a) $c_w = 0$; (b) $c_w = 0.01$; (c) $c_w = 0.1$; d) $c_w = 1$.

the purely hydrodynamic case, Fig. 3(b), and basically due to the impingement of the turning boundary layer on the vertical cold wall, is greatly reduced, and the distribution of q'' becomes more uniform, as the Hartmann number increases (graphs ((a) to (d)).

4.4. The effect of the wall conductance ratio c_w

For *differentially* heated enclosures, previous studies [4,20] have shown that the wall conductance ratio plays a major role in determining the current distribution, the flow patterns and the heat transfer characteristics. For *internally* heated enclosures, a similar major influence was observed in fully developed buoyant flows [2].

A vector plot of the current density **j** in the horizontal midplane $z = 0$ of the cubic enclosure is shown in Fig. 11 for $M = 100, Ra = 10^5$, and insulating ($c_w = 0$) or perfectly conducting ($c_w \to \infty$) walls. For non-conducting walls, graph (a), high currents flow through the side layers, parallel to **B**, as already observed in the fully developed study [2]. This pattern is observed up to $c_w \approx 0.01$. For well conducting walls, graph (b), currents exit orthogonally from the right regions of the Hartmann walls, describe a 180° turn in the fluid domain and enter again the Hartmann walls on the left side. This pattern is observed for $c_w \geqslant 0.1$.

Fig. 12 reports velocity vector plots in the midplane $y = 0$ orthogonal to the magnetic field **B**; the horizontal arrow reported above each graph represents the (dimensionless) unity velocity vector. The magnetic field causes an increasing suppression of the flow in the centre of the cavity for increasing wall conductance ratio (graphs (a)–(d)), as compared with the case without MHD interactions in Fig. 2(a). As in the differentially heated enclosures, the increasing Lorentz forces (from graph (a) to (d)) give rise to an increasingly square shape of the circulation pattern.

Fig. 13(a) reports profiles of the vertical velocity w along the x axis. It can be observed that the base third-order polynomial profile of w, derived analytically for

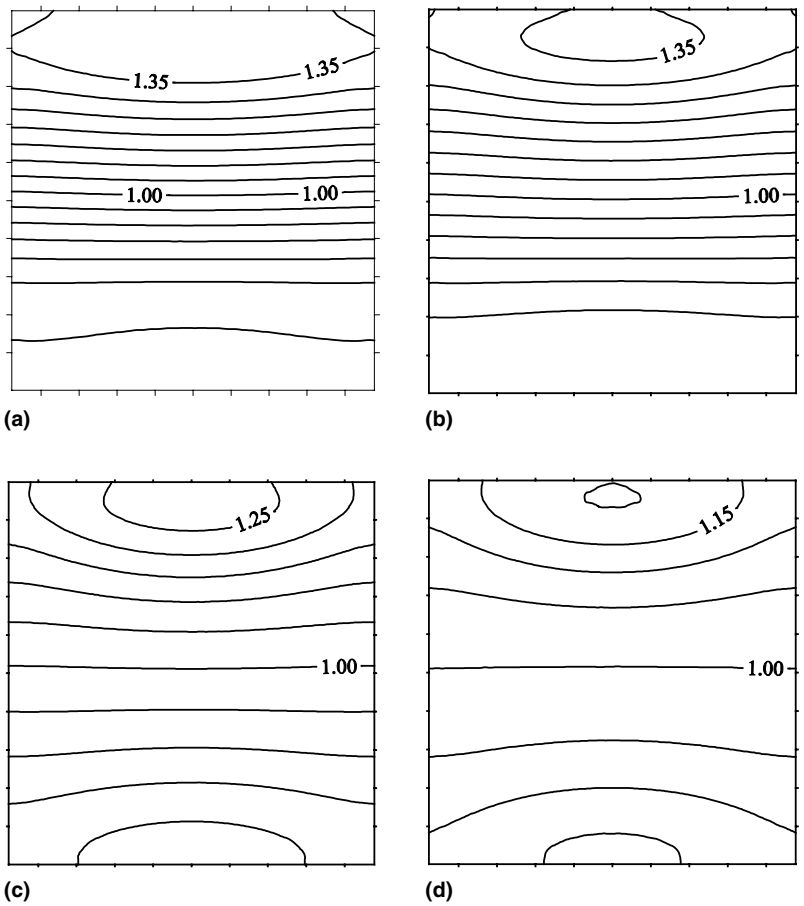

Fig. 15. Distribution of $q''/\langle q''\rangle$ on a cooling wall for $M = 100$, $Ra = 10^5$. Velocities for "no MHD" are scaled as for $M = 100$. (a) $c_w = 0$; (b) $c_w = 0.01$; (c) $c_w = 0.1$; (d) $c_w = 1$.

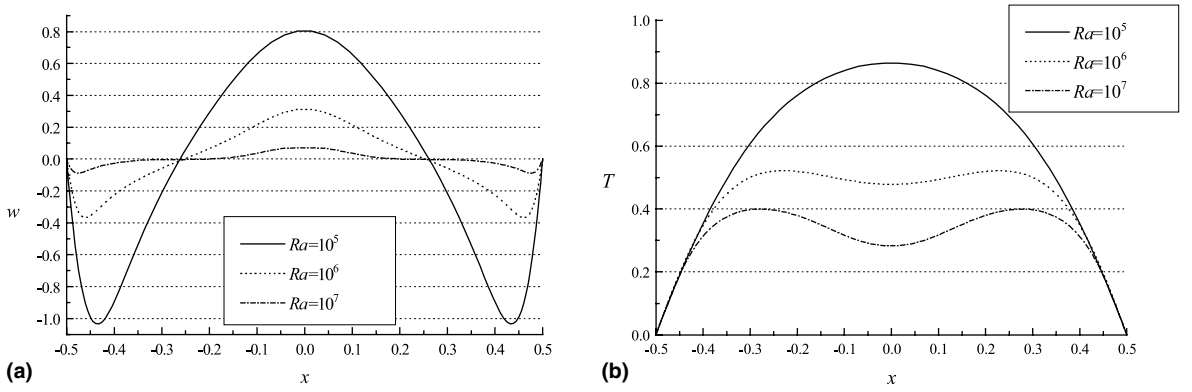

Fig. 16. Dimensionless w velocity (a) and temperature (b) profiles along the x axis for $M = 100$, $c_w = 0.01$ and three values of the Rayleigh number ($Ra = 10^5,\ 10^6,\ 10^7$).

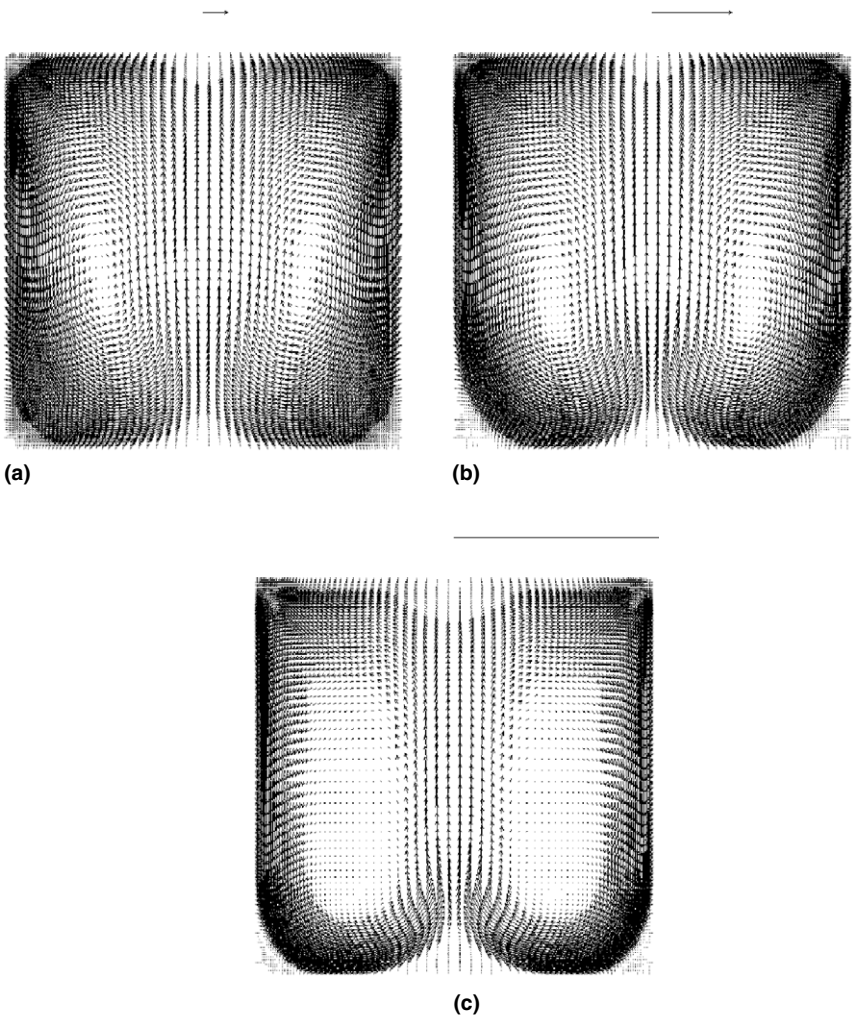

Fig. 17. Velocity vectors in the midplane $y = 0$ for $c_w = 0.01$, $M = 100$. The unity (dimensionless) vector is shown close to each plot. Different scales are used for (a), (b), (c). (a) $Ra = 10^5$; (b) $Ra = 10^6$; (c) $Ra = 10^7$.

infinitely slender enclosures [9] in the absence of MHD effects, is almost preserved for the lower values of c_w, while, for higher c_w, profiles of w become almost flat in the core region due to the strong Lorentz forces. Conversely, the temperature profiles in Fig. 13(b) show that the purely conductive parabolic distribution is still preserved for well conducting walls, while convection is stronger for poorly conducting walls, and a progressive reduction of the temperature maximum occurs. This effect can be also observed in the temperature fields shown in Fig. 14 for the midplane $y = 0$: for the higher values of c_w (graphs (c) and (d)) vertical thermal stratification is almost absent, and the dominant horizontal T gradient indicates a quasi-conductive solution. For the lower c_w (graphs (a) and (b)) the solution is closer to that obtained without MHD interactions, Fig. 3(a), with a stronger vertical stratification at least in the upper region of the enclosure.

Fig. 15 shows the heat flux distribution on one of the cold walls; q'' is normalized by its mean value $qD/2$. The distribution tends to be flatter and more top/down symmetric for increasing c_w, as magnetic interactions become stronger.

4.5. The effect of the Rayleigh number Ra

For fixed values of the Hartmann number ($M = 100$) and of the wall conductance ratio ($c_w = 0.01$), the Rayleigh number was made to vary from 10^5 to 10^7. It should be observed that two-dimensional direct simulations conducted for an internally heated square cavity in the absence of MHD effects [13] gave steady but asymmetric flow for $Ra = 10^6$, and chaotic flow for $Ra = 10^7$. However, the damping effects of the magnetic field at $M = 100$ seem to be sufficient to stabilize steady symmetric free convection flow at these values of the Rayleigh number; the present simulations, conducted by imposing steady-state conditions and including the whole cubic enclosure, neither exhibited convergence problems nor any tendency to break the flow symmetry.

Fig. 16 reports profiles of dimensionless vertical velocity w (a) and temperature T (b) along the x axis for

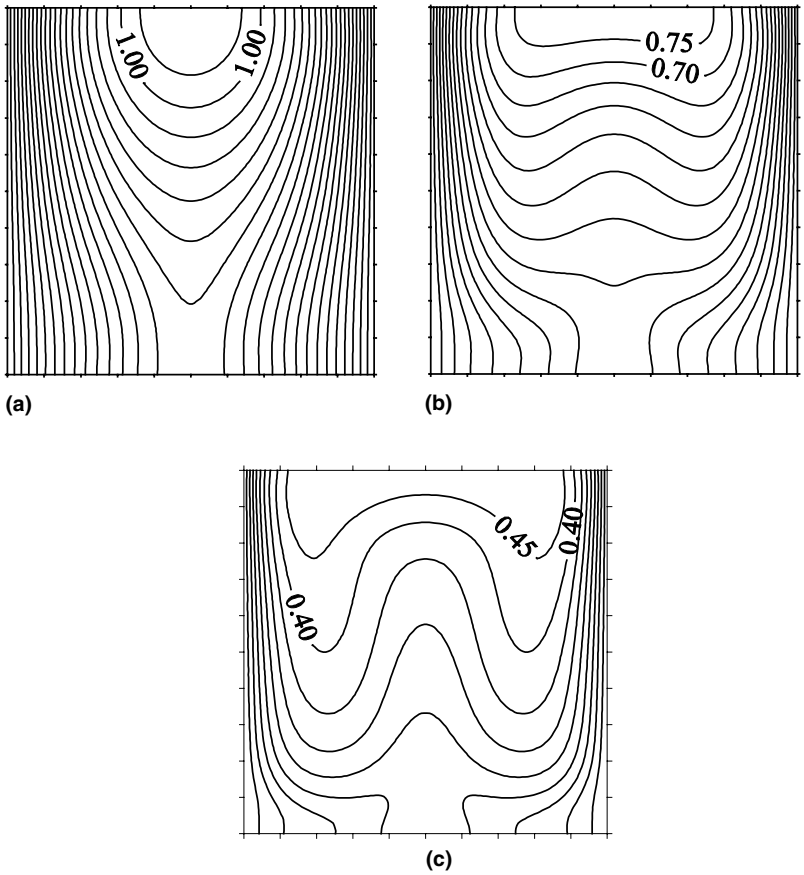

Fig. 18. Dimensionless temperature fields in the midplane $y = 0$ for $c_w = 0.01$, $M = 100$ and different values of the Rayleigh number. (a) $Ra = 10^5$; (b) $Ra = 10^6$; (c) $Ra = 10^7$.

the three values of Ra investigated. The strong decrease of w with increasing Ra suggests that the scale adopted here for velocity, $u_0 = (\alpha/D)(Ra/M^2)$, is not really suitable when convective transport becomes dominant; in fact, velocities scale better with $Ra^{1/2}$ rather than with Ra. The third-order polynomial profile of w, still recognizable for $Ra = 10^5$, is progressively lost as the central rising plume and the near-wall downcoming boundary layers become increasingly de-coupled. Fig. 17 shows velocity vector plots in the midplane $y = 0$ for $Ra = 10^5$–10^7; as Ra increases, convection becomes increasingly confined to thin near-wall boundary layers and the centres of the circulation cells move downwards.

The temperature maximum is reduced for the higher values of Ra, as shown in Fig. 16(b); furthermore, the shape of the T profile is strongly modified and a relative minimum appears about the midplane $x = 0$. The importance of convection and thermal mixing at high Ra, despite the damping effect of magnetohydrodynamics, is also evidenced in Fig. 18, which reports temperature contour plots in the midplane $y = 0$. For the higher Ra (graphs (b) and (c)) the isotherms are strongly distorted by convection, which explains the relative minimum present in the midline temperature distribution of Fig. 16(b).

Finally, the distribution of the normalized heat flux on a cooling wall is shown in Fig. 19. A maximum of heat transfer can be observed in the top region, where the downcoming side boundary layer begins to develop; this maximum is exalted for the higher Ra.

The resulting Nusselt numbers for the cases under consideration increase with Ra, and are summarised in Table 1. Following our previous work on 2-D enclosures with internal heat generation [13], Nu_1 and Nu_2 are defined as $1/T_{\max}$ and $(2/3)/\langle T\rangle$, respectively, so that they are both unity for a purely conductive temperature distribution and otherwise express the relative importance of convection with respect to conduction. The convection-driven accumulation of hot fluid against the top wall of the enclosure is responsible for the Nusselt number $Nu_1 < 1$, obtained at the lowest Rayleigh number. Despite MHD flow damping effects, the Nusselt

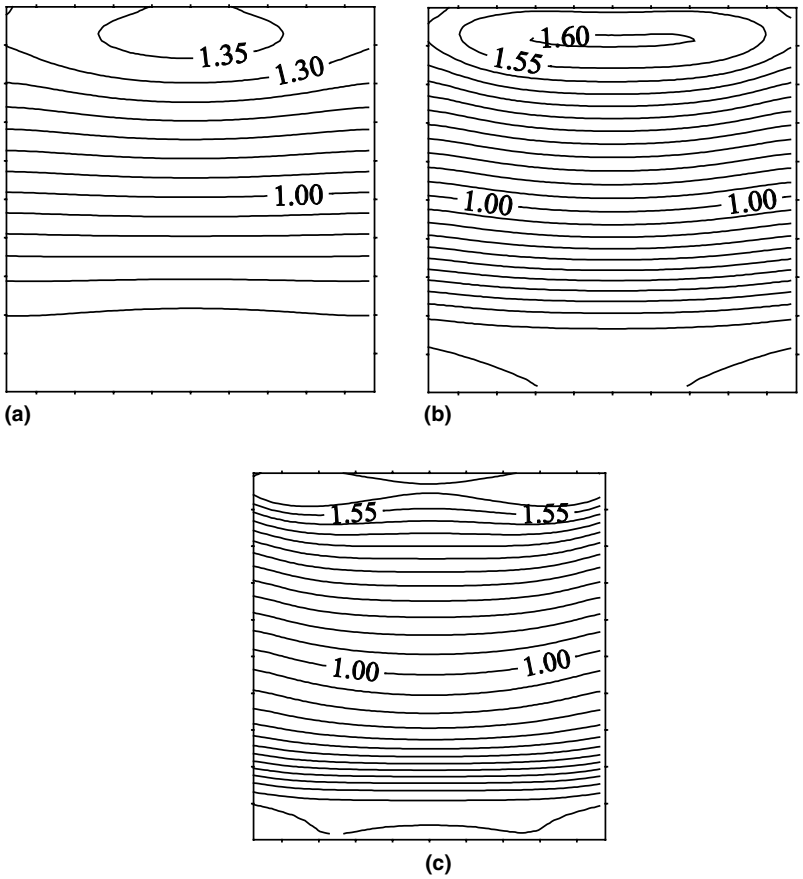

Fig. 19. Distribution of $q''/\langle q''\rangle$ on a cooling wall for $c_w = 0.01$, $M = 100$ and different values of the Rayleigh number. (a) $Ra = 10^5$; (b) $Ra = 10^6$; (c) $Ra = 10^7$.

Table 1
Influence of the Rayleigh number on the Nusselt numbers for an internally heated enclosure with $c_w = 10^{-2}$, $M = 100$

Ra	$Nu_1 = 1/T_{max}$	$Nu_2 = (2/3)/\langle T \rangle$
10^5	0.909	1.084
10^6	1.251	1.546
10^7	1.919	2.195

numbers computed for $Ra = 10^7$ ($\sim$2) are comparable with those obtained for the same Rayleigh number in two-dimensional direct, time-dependent simulations without MHD interactions in a square cavity [9,13].

5. Conclusions

Three-dimensional numerical simulations were conducted for the MHD buoyancy-driven flow in a volumetrically heated cubic enclosure using a suitably modified version of the CFX-4 software. The study was motivated by the need for a better understanding of the thermal-hydraulics phenomena occurring in water-cooled lithium-lead breeder blankets for commercial fusion reactors, where internal heat generation and MHD interactions occur simultaneously. However, the configuration studied is a basic one which may also be of interest in different fields of physics and engineering. The computational method adopted in the present study is quite general and can easily be extended to more complex configurations.

In the cubic enclosure, with respect to the fully developed flow problem studied in previous work, the suppression of the flow field was stronger in the core, and a complex three-dimensional flow (with secondary motions) and current pattern was established in the fluid domain. The effects of Hartmann number, wall conductance ratio and Rayleigh number were investigated.

Increasing the Hartmann number tended to suppress the convective motions and to make the circulation cells more square in shape and more uniform spanwise; MHD forces tended to align vorticity with the direction of the magnetic field. Increasing the wall conductance ratio c_w from insulating to perfectly conducting walls also resulted in a significant increase of MHD damping effects. For poorly conducting walls, intense current jets were predicted to flow through the side layers parallel to **B**, as already observed in the fully developed study.

For $M = 100$ and $c_w = 10^{-2}$, as the Rayleigh number increased from 10^5 to 10^7 the Nusselt numbers increased from $\sim$1 to $\sim$2. This latter value is comparable to that obtained for the same Rayleigh number in two-dimensional direct simulations of free convection in an internally heated square cavity without MHD interactions, for which a chaotic behaviour was observed. This suggests the possibility of obtaining high convective heat transfer rates, while keeping the flow within the steady laminar range, by making use of MHD effects.

The related case of a cubic enclosure with *differential* heating is the subject of a companion paper [4].

References

[1] F. Carré, E. Proust, J. Remolouv, A. Racaboy, Z. Tilliette, Fusion reactor blanket – comparative evaluation study, Report EMT/SERMA/BP/84/No. 584 T, 3591-21-000, 1984.
[2] I. Di Piazza, L. Bühler, A general computational approach for magnetohydrodynamic flows using the CFX code: buoyant flow through a vertical square channel, Fusion Technol. 38 (2) (2000) 180–189.
[3] L. Bühler, Laminar buoyant magnetohydrodynamic flow in vertical rectangular ducts, Phys. Fluids 10 (1) (1998) 223–236.
[4] I. Di Piazza, M. Ciofalo, MHD free convection in a liquid-metal filled cubic enclosure. I. Differential heating, Int. J. Heat Mass Transfer 45 (7) (2002) 1477–1492.
[5] R. Moreau, Magnetohydrodynamics, Kluwer Academic Publishers, Amsterdam, 1990.
[6] J.S. Walker, Magnetohydrodynamic flows in rectangular ducts with thin conducting walls, J. Méch. 20 (1) (1981) 79–112.
[7] J.R. Van Doormal, G.D. Raithby, Enhancements of the SIMPLE method for predicting incompressible flows, Numer. Heat Transfer 7 (1981) 147–163.
[8] CFX-4.2: Solver, CFX-International, Harwell Laboratories, UK, 1997.
[9] I. Di Piazza, Prediction of free convection in liquid metals with internal heat generation and/or magnetohydrodynamic interactions, Doctoral Thesis, University of Palermo, 2000.
[10] L. Leboucher, Numerical simulation of unsteady magnetohydrodynamic flows in ducts, Technical Report FZKA 5663, Forschungszentrun Karlsruhe, 1995.
[11] L. Bühler, Magnetohydrodynamic flows in arbitrary geometries in strong, nonuniform magnetic fields – a numerical code for the design of fusion reactor blankets, Fusion Technol. 27 (1994) 3–24.
[12] F.A. Kulacki, D.E. Richards, Natural convection in plane layers and cavities with volumetric energy sources, in: S. Kakaç, W. Aung, R. Viskanta (Eds.), Natural Convection – Fundamentals and Applications, Hemisphere, New York, 1985, pp. 179–254.
[13] S. Arcidiacono, I. Di Piazza, M. Ciofalo, Low-Prandtl number natural convection in volumetrically heated rectangular enclosures. II. Square cavity, $AR = 1$, Int. J. Heat Mass Transfer 44 (3) (2001) 537–550.
[14] S.H. Davis, J. Fluid Mech. 30 (1967) 465.
[15] G.D. Mallinson, G. de Vahl Davis, Three-dimensional natural convection in a box: a numerical study, J. Fluid Mech. 83 (1977) 1–31.
[16] W.J. Hiller, St. Koch, T.A. Kowalewski, Three-dimensional structures in laminar natural convection in a cube shaped enclosure, in: P.K. Shah, E.N. Ganiç, K.T. Yang (Eds.), Experimental Heat Transfer, Fluid Mechanics, and Thermodynamics 1988, Elsevier, Amsterdam, 1988, pp. 722–729.

[17] R.J.A. Janssen, R.A.W.M. Henkes, C.J. Hoogendoorn, Transition to time-periodicity of a natural-convection flow in a 3D differentially heated cavity, Int. J. Heat Mass Transfer 36 (11) (1993) 2927–2940.

[18] R.A.W.M. Henkes, P. Le Quéré, Three-dimensional transition of natural-convection flows, J. Fluid Mech. 319 (1996) 281–303.

[19] U. Müller, L. Bühler, Magnetohydrodynamic flows in ducts and cavities, in: Proceedings of the IUTAM 99 Summer School on Liquid Metal MHD, Udine, Italy, 1999.

[20] T. Tagawa, H. Ozoe, The natural convection of liquid metal in a cubical enclosure with various electro-conductivities of the wall under the magnetic field, Int. J. Heat Mass Transfer 41 (1998) 1917–1928.